

Low-loss Transmission Lines for High-power Terahertz Radiation

Emilio Alessandro Nanni · Sudheer Kumar Jawla ·
Michael A. Shapiro · Paul P. Woskov · Richard J. Temkin

Received: 21 October 2011 / Accepted: 3 January 2012 /
Published online: 1 February 2012
© Springer Science+Business Media, LLC 2012

Abstract Applications of high-power Terahertz (THz) sources require low-loss transmission lines to minimize loss, prevent overheating and preserve the purity of the transmission mode. Concepts for THz transmission lines are reviewed with special emphasis on overmoded, metallic, corrugated transmission lines. Using the fundamental HE_{11} mode, these transmission lines have been successfully implemented with very low-loss at high average power levels on plasma heating experiments and THz dynamic nuclear polarization (DNP) nuclear magnetic resonance (NMR) experiments. Loss in these lines occurs directly, due to ohmic loss in the fundamental mode, and indirectly, due to mode conversion into high order modes whose ohmic loss increases as the square of the mode index. An analytic expression is derived for ohmic loss in the modes of a corrugated, metallic waveguide, including loss on both the waveguide inner surfaces and grooves. Simulations of loss with the numerical code HFSS are in good agreement with the analytic expression. Experimental tests were conducted to determine the loss of the HE_{11} mode in a 19 mm diameter, helically-tapped, three meter long brass waveguide with a design frequency of 330 GHz. The measured loss at 250 GHz was 0.029 ± 0.009 dB/m using a vector network analyzer approach and 0.047 ± 0.01 dB/m using a radiometer. The experimental results are in reasonable agreement with theory. These values of loss, amounting to about 1% or less per meter, are acceptable for the DNP NMR application. Loss in a practical transmission line may be much higher than the loss calculated for the HE_{11} mode due to mode conversion to higher order modes caused by waveguide imperfections or miter bends.

E. A. Nanni (✉) · S. K. Jawla · M. A. Shapiro · P. P. Woskov · R. J. Temkin
Plasma Science and Fusion Center, Massachusetts Institute of Technology, Cambridge,
MA 02139, USA
e-mail: enanni@mit.edu

Keywords Terahertz · High power · Transmission line · Waveguide · Gyrotron

1 Introduction

Transmission of high-power THz radiation has proved challenging due to the lossy nature of most fundamental mode transmission lines at these frequencies. Both material properties as well as machining tolerances contribute to the limitations imposed on fundamental rectangular or circular waveguide which is often the preferred approach at lower frequencies (GHz range). An overmoded approach to transmission lines has been demonstrated as an efficient and practical solution for high-power THz applications [1–8]. The number of approaches to the design of overmoded transmission lines is quite extensive. Free space beaming techniques rely on propagation of a Gaussian beam via a series of mirrors and/or lenses [9–11]. This approach has low-loss but may have issues of safety and alignment stability. The most common approach is the use of overmoded waveguides, in which the guide radius is much larger than the wavelength. Such waveguides can be corrugated metallic waveguides, dielectric waveguides or dielectric lined metallic waveguides. Free space beaming and corrugated waveguide are closely related, because the fundamental HE_{11} mode used in corrugated waveguides has a conversion efficiency of 98% [12] to the Gaussian beam which is used in quasi-optical transmission. Extensive reviews of the properties of overmoded waveguides have been published [13, 14] for sub-THz and megawatt power level transmission lines. High-power sub-THz transmission lines have been rigorously tested for use in electron cyclotron resonance heating (ECRH) of plasma experiments such as DIII-D [15], ASDEX [16] and LHD [17]. With further research being driven by ITER [18–21], this remains an active area of interest. With overmoded transmission lines, ohmic losses play a greatly reduced role; however, special attention is required to sources of mode conversion caused by misalignments and offsets. Mode conversion to higher order modes results in increased losses, reflections and greatly reduced coupling of the THz radiation to the desired target or sample. Overmoded corrugated waveguides have been used in a variety of applications for the transmission of THz radiation for spectroscopic and plasma heating experiments. The HE_{11} mode is the most efficient waveguide propagation mode in an overmoded corrugated metallic waveguide with a diameter $\gg 2\lambda$, and having internal circumferential corrugations of rectangular shape with a depth of $\lambda/4$ at a pitch of at least 2.5 grooves per λ along the waveguide length [22, 23].

Low-loss broad band transmission lines are of great interest for low power THz spectroscopy and imaging [24, 25]. To overcome the extremely high losses of simple rectangular or circular waveguides, a variety of different methods are being investigated including dielectric coated metallic tubes [26], dielectric waveguides [27, 28], metallic wires [29], parallel metallic plates [30] and photonic crystals [31, 32]. Using dielectric lined metal waveguides, a loss

of 1 dB/m has been achieved at frequencies above 1 THz [33]. Many of these techniques employ the use of overmoded waveguides and strive to find modes that can be efficiently coupled to free space THz beams. Currently, these techniques yield losses that are too high for continuous wave (CW) systems with high average power and for systems with transmission lines on the order of multiple meters.

Electron cyclotron emission (ECE) diagnostics on plasma fusion experiments are now requiring the development of transmission lines in the THz band. ECE can be observed at either the fundamental or harmonics of the electron cyclotron frequency, $\omega = neB/m$, where m and e are the electron mass and charge, B is the magnetic field and $n = 1, 2, 3, \dots$ is the harmonic number. With the magnetic field varying significantly within the fusion plasma, these diagnostics require broadband transmission lines for observation of ECE. Additionally, observation at harmonics of the electron cyclotron frequency provide the advantage of not receiving direct interference from the ECRH system that could be active. Frequency selective transmission line components have been developed for direct observation of ECE at ~ 140 GHz on the ECRH transmission line at TEXTOR [34]. Similar systems are under consideration for ASDEX [35] and ITER [36], which will require operation at higher frequencies. The ITER ECE diagnostic will operate independently of the ECRH transmission line and will observe emission from the plasma at frequencies as high as 0.35 THz [37–39].

In the THz range (>300 GHz), research into high-power (>10 W) transmission lines is being driven by dynamic nuclear polarization (DNP) nuclear magnetic resonance (NMR) experiments which require low-loss and a minimum of mode conversion [40]. For these experiments, the gyrotron and DNP magnets must be sufficiently far apart to avoid mutual field interference [1], requiring transmission of THz radiation over a distance of several meters [8]. It is not possible to use conventional single mode rectangular waveguides for transmission, since the ohmic loss in such guides would be prohibitive. Modern gyrotrons for DNP typically include internal mode converters [41–45] after the interaction region of the gyrotron to transform the THz radiation from the high order TE_{mn} mode in the cavity to a Gaussian beam. For gyrotrons without internal mode converters, alternate configurations can include quasi-optical mode converters external to the gyrotron [5] which produce Gaussian beams. The Gaussian beam then propagates through the dielectric output window of the gyrotron where it can be coupled either to a corrugated waveguide or the quasi-optical setup. The linearly polarized Gaussian beam excites the linearly polarized HE_{11} mode in the waveguide [46]. Then it is convenient to transmit the HE_{11} mode to the sample under study with straight sections, miter bends and tapers of corrugated metallic waveguide.

As NMR experiments move to higher field, the frequency that must be transmitted extends further into the THz band. Due to the scaling of the groove size with wavelength, this requires smaller corrugations. Machining individual corrugations becomes increasingly difficult and expensive as the corrugation dimensions shrink with frequency. The machining process necessitates the

assembly of many short sections of waveguide. To avoid these machining considerations, creating corrugations with stacked rings has been attempted [3]. Alternatively, tapping a single helical groove is more cost effective for making long sections of corrugated waveguide.

In this paper, we review the design of low-loss corrugated waveguides in Section 2; Section 3 derives the ohmic losses in corrugated waveguides; Section 4 describes simulations for the calculation of ohmic losses with non-ideal groove shapes; Section 5 describes the fabrication of helically-tapped corrugated waveguide; Section 6 presents ohmic loss measurements performed on corrugated waveguide; Section 7 is the summary and conclusions.

2 High-power low-loss corrugated metallic THz transmission lines

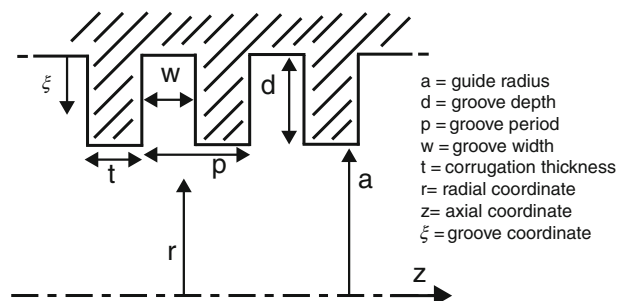
Figure 1 shows a schematic of a corrugated metallic waveguide with rectangular grooves. The radius a is much larger than a wavelength λ . The corrugations are optimized when the groove depth $d \approx \lambda/4$, period $p \approx \lambda/3$ and groove width $w < p/2$. The corrugation tooth thickness is denoted by $t = p - w$. The radial coordinate r extends from the center line of the waveguide and the groove coordinate ξ originates from the base of the groove well. The axial coordinate z is parallel to the centerline.

The modes in a corrugated waveguide have been developed [23], with the lowest order mode being the HE_{11} hybrid mode. The transverse electric field profile near the optimized groove depth $d \approx \lambda/4$ is given by:

$$E^{mn}(r, \phi) = (\chi_{mn}/a) J_m(\chi_{mn}r/a) \cos(m\phi) \quad (1)$$

where (r, ϕ) are the radial and angular coordinates and χ_{mn} is the n^{th} zero of the m^{th} order Bessel function J_m . For the HE_{11} mode $m = 0, n = 1$ and $\chi_{01} \approx 2.405$. This expression is valid when the corrugation depth is approximately one quarter wavelength and the radius a is much larger than the wavelength. For perfect excitation of the HE_{11} mode in the transmission line, the overall transmission line loss is expected to be dominated by losses at right angle bends, called miter bends, and by tilts and offsets in the fabrication and alignment of the waveguide components. The loss in a miter bend originates

Fig. 1 Illustration of a corrugated metallic waveguide which is optimized with a radius $a \gg \lambda$, groove depth $d \approx \lambda/4$, period $p \approx \lambda/3$ and groove width $w < p/2$.



from diffraction effects and ohmic losses, with the fractional power loss from diffraction

$$P_{\text{Diffraction}} = 0.195 \left(\frac{\lambda}{a \sin \theta} \right)^{3/2}, \tag{2}$$

ohmic losses in H-plane miter bends

$$P_{\text{Ohmic}} = \frac{4R_s \cos \alpha}{Z_0}, \tag{3}$$

and E-plane miter bends

$$P_{\text{Ohmic}} = \frac{4R_s}{Z_0 \cos \alpha} \tag{4}$$

where R_s is the surface resistivity, Z_0 is the impedance of free space, θ is the bend angle and α is the angle of incidence [14, 47]. Fabrication of overmoded corrugated waveguide components requires careful consideration of machining tolerances at the waveguide connections. Tilts and axial offsets can lead to the coupling of the input THz beam to higher order modes of the waveguide, which gives rise to mode conversion losses, resulting in an increase of ohmic losses or decreased coupling to the sample of interest. The fractional power loss due to mode conversion [12, 14] for an axial offset, Δa , is

$$P_{\text{Offset}} = 2.7 \left(\frac{\Delta a}{a} \right)^2, \tag{5}$$

and for a tilt, $\Delta \theta$, is

$$P_{\text{Tilt}} = 4.2 \left(\frac{a \cdot \Delta \theta}{\lambda_0} \right)^2. \tag{6}$$

While these are significant sources of loss, in practice the loss may be dominated by the imperfections and poor coupling of the THz beam entering the transmission line, resulting in the excitation of higher order modes. This is a result of the non-Gaussian output beam either from the source or upon insertion of an unmatched output beam (due to tilts and offsets) into the waveguide, leading to high losses in the transmission line [21].

Figure 2a shows the transmission line used in a 250 GHz DNP NMR system [1]. The main transmission line is a 22 mm diameter ($a = 11$ mm) metallic corrugated waveguide made of aluminum. The individually machined corrugations are optimized with $d \approx \lambda/4$ (0.3 mm), $w = 0.3$ mm and $p = 0.4$ mm. Two 0.254 m waveguide sections, fifteen 0.124 m waveguide sections and one 0.064 m directional coupler block were assembled with outer diameter clamps to achieve the desired waveguide length. The difference between the measured and theoretical loss is discussed in detail in Section 6. The estimated ohmic loss in the overmoded waveguide of Fig. 2a is less than 10^{-3} /m. The loss for the 22 mm diameter waveguide portion of the transmission line of Fig. 2a was measured to be less than 1% per meter [1].

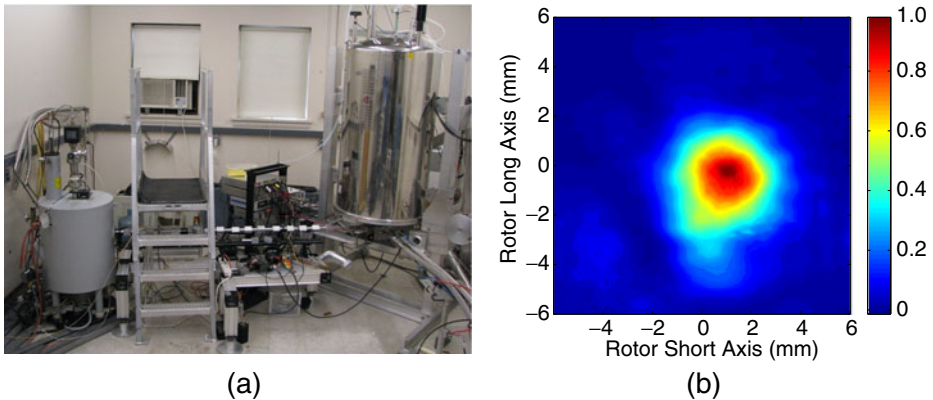


Fig. 2 (a) The 250 GHz transmission line connecting the gyrotron output (*left*) to the NMR spectrometer (*right*). (b) The measured Gaussian beam emitted from the end of an 8 mm corrugated waveguide and radiated to a distance of 12 mm from the waveguide end.

A directional coupler is used for measuring forward and reverse power on the transmission line shown in Fig. 2a. A smaller diameter waveguide is necessary for the probe inside the DNP NMR magnet due to limited space. The transition to smaller diameter can be performed with waveguide tapers or mirrors. Bends in the transmission line may be accomplished using a miter bend in the waveguide or using a mirror box. The transmission line of Fig. 2a has only one right angle bend, and it is implemented using two mirrors. The mirrors also match the beam from the 22 mm waveguide into the 8 mm waveguide in the NMR probe. Due to losses induced by imperfections in the Gaussian beam quality of the gyrotron and by errors in the alignment of the components of the transmission line, the transmission efficiency from the gyrotron output window to the sample is typically in the 50–80% range [1, 48] measured at the 8 mm corrugated waveguide output that radiates onto the sample. Figure 2b is an image of the beam radiated to the sample distance of 12 mm from the end of the corrugated waveguide recorded using a Spiricon Pyrocam III pyroelectric detector.

The transmission line shown in Fig. 2 is only one example of successful transmission lines used in DNP NMR research. Recently, a 13 m transmission line using corrugated waveguides and switches has been successfully implemented on a 260 GHz gyrotron system for DNP NMR [4, 5]. A fully optical (mirror) transmission line using a mirror relay line has also recently been implemented for a DNP NMR spectrometer system [49]. Another overmoded smooth-walled waveguide has been successfully implemented at 395 GHz [50] with 55% transmission on a 28 mm diameter waveguide to the base of the DNP magnet and 7% of the output power delivered to the sample. A recently implemented 460 GHz transmission line for DNP applications [2, 51, 52] has been tested with 40% transmission of power to the sample. The 460 GHz transmission line, shown in Fig. 3a, is constructed using the same techniques

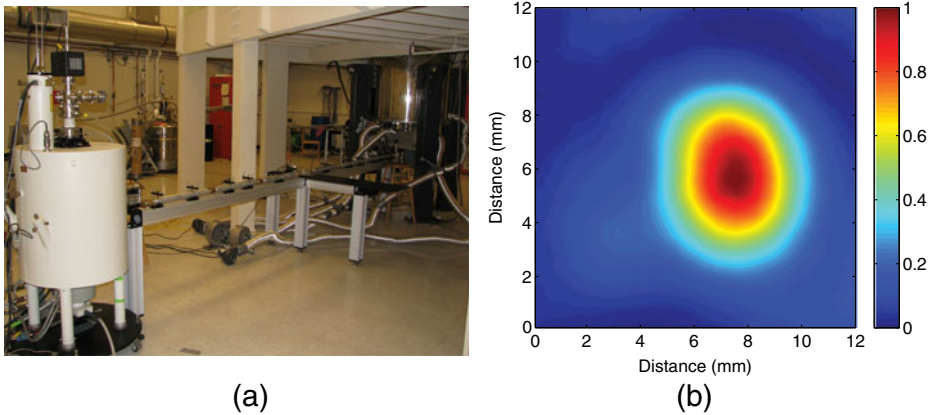


Fig. 3 (a) The 460 GHz transmission line connecting the gyrotron output (*left*) to the NMR spectrometer (*right*). (b) The measured Gaussian beam emitted from the end of a 19 mm ID corrugated waveguide and radiated to a distance of 10 cm from the waveguide end.

as the 250 GHz transmission line, shown in Fig. 2a, and consists of a 6 m long, 19 mm diameter corrugated waveguide, which is tapered to a diameter of 4.6 mm once it reaches the probe. The field pattern shown in Fig. 3b was measured using a Spiricon Pyrocam III pyroelectric detector positioned 10 cm from the aperture of the waveguide at the center point between the gyrotron magnet and NMR spectrometer. Future research will concentrate on making these transmission lines simpler and more efficient.

3 Theory of ohmic losses in corrugated waveguides

Selection of waveguide radius and groove dimensions has severe effects on the ohmic loss in corrugated waveguides, requiring careful understanding of the source of attenuation in these waveguides. Here we derive an analytical formula for the attenuation coefficient of a corrugated metallic waveguide with ideal rectangular grooves. The result was obtained by integrating the field equations over the groove surfaces to obtain the ohmic loss. The electric and magnetic fields of the HE mode at $r = a$ are [23]

$$\mathbf{E}(r = a, \phi) = \mathbf{e}_{01} = -\left(\frac{Z_0}{\pi}\right)^{1/2} \frac{\chi_m}{ka^2} \left[\hat{r} \frac{1}{Z} - j\hat{z} \right] \sin \phi \tag{7}$$

$$\mathbf{H}(r = a, \phi) = \mathbf{h}_{01} = -\left(\frac{1}{Z_0\pi}\right)^{1/2} \frac{\chi_m}{ka^2} \left[\hat{\phi} \frac{\sin \phi}{Z} - j \cos \phi \hat{z} \right] \tag{8}$$

where the unit vectors for $r/\phi/z$ are $\hat{r}/\hat{\phi}/\hat{z}$, Z_0 is the impedance of free space, $Z = \frac{w}{p} \tan kd$ is the approximate impedance seen at the corrugated surface, $k = 2\pi/\lambda$ is the wavenumber, $\chi_m = \chi_{01} (1 - 1/2kaZ)$ [22] and $ka \gg 1$. To

calculate the attenuation constant for the waveguide we integrate the ohmic losses over the groove shape of one period [53, 54]

$$\alpha = \frac{R_s}{2} \frac{1}{p} \iint (|H_\phi|^2 + |H_z|^2) dsd\phi \tag{9}$$

where ds denotes the surface of the groove, $R_s = \sqrt{\pi\mu\rho f}$ is the surface resistivity, μ is the permeability, f is the frequency, ρ is the bulk resistivity and α has units of Np/m. In the traditional approach, we can rewrite Eq. 9 in terms of the fields from Eq. 8 and integrate over a flat surface which is represented by the approximate impedance [23]

$$\alpha = \frac{R_s}{2} \frac{1}{p} \int_0^{2\pi} \int_0^p (|h_\phi|^2 + |h_z|^2) adzd\phi. \tag{10}$$

The result is given by [23]

$$\alpha = \frac{R_s}{2Z_0} \frac{\chi_m^2}{k^2 a^3} \left(\frac{1}{(w/p)^2 \tan^2 kd} + 1 \right). \tag{11}$$

To improve this calculation, the integral in Eq. 9 should be performed over the entire surface of the groove, where Eq. 8 is not strictly valid. In [53] this is remedied by using a spatial harmonics representation for the fields inside the waveguide and an infinite set of resonant modes inside the corrugations. Alternatively, we allow for H_ϕ to be at a maximum and $E_z = 0$ at the base of the groove ($\xi = 0$) for $d \approx \lambda/4$. To satisfy boundary conditions we take $H_\phi = h_\phi \frac{\cos k\xi}{\cos kd}$ for $0 \leq \xi \leq d$. For the z component it is sufficient to calculate the loss on the surface $r = a$ where $H_z = h_z$, which is the same approach used in the impedance approximation method. This leads to the integration

$$\alpha = \frac{R_s}{2} \frac{1}{p} \left[\iint \left| h_\phi \frac{\cos k\xi}{\cos kd} \right|^2 dsd\phi + ap \int_0^{2\pi} |h_z|^2 d\phi \right]. \tag{12}$$

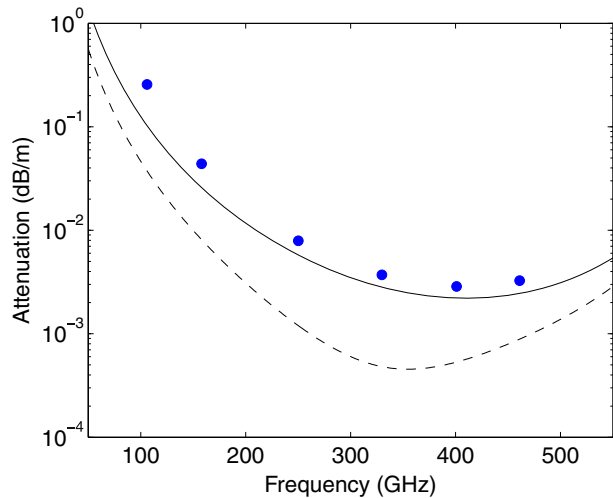
If we separate Eq. 12 into the different surfaces of the rectangular groove

$$\alpha = \frac{R_s}{2} \frac{1}{p} \left[2 \int_0^{2\pi} \int_0^d \left| h_\phi \frac{\cos k\xi}{\cos kd} \right|^2 ad\xi d\phi + \int_0^{2\pi} \int_0^w \left| h_\phi \frac{1}{\cos kd} \right|^2 adzd\phi + \int_0^{2\pi} \int_0^t |h_\phi|^2 adzd\phi + ap \int_0^{2\pi} |h_z|^2 d\phi \right] \tag{13}$$

and perform the integrations, the attenuation is given by

$$\alpha = \frac{R_s}{2Z_0} \frac{\chi_m^2}{k^2 a^3} \left[\frac{1}{Z^2 p} \left(2 \frac{1}{\cos^2 kd} \left(\frac{d}{2} + \frac{1}{2k} \sin kd \cos kd \right) + \frac{w}{\cos^2 kd} + t \right) + 1 \right], \tag{14}$$

Fig. 4 Ohmic losses in overmoded circular corrugated waveguide for rectangular brass (conductivity 1.56×10^7 mhos/m) corrugations as predicted by our theory (solid line) and the impedance approximation method (dashed line). Numerical simulations with HFSS are shown with blue dots.



which can be further simplified in terms of the expression given by

$$\alpha = \frac{R_s}{2Z_0} \frac{\chi_m^2}{k^2 a^3} \left(\frac{1 - \frac{t}{p} \sin^2(kd) + \frac{d}{p} + \frac{1}{kp} \sin(kd) \cos(kd)}{(1 - t/p)^2 \sin^2(kd)} + 1 \right). \tag{15}$$

Equation 15 shows that the loss increases as the square of the mode index χ_m . Thus, mode conversion into high order modes, with large χ_m , can contribute to greatly enhanced loss on a transmission line. A comparison between (11) (dashed black line) and Eq. 15 (solid black line) is shown in Fig. 4 for the HE_{11} mode with rectangular corrugations, $a = 9.5$ mm, $d = 0.227$ mm, $p = 0.3175$ mm, $t/p = 0.5$ and ideal brass conductivity. The figure shows attenuation in dB/m which can be obtained from the attenuation in Np/m multiplied by 8.686. As d approaches $\lambda/4$, a significant difference develops between Eq. 11 (dashed line) and Eq. 15 (solid line) because the contribution from h_ϕ goes to zero in Eq. 11 and losses internal to the corrugations are not accounted for as in Eq. 15. It should be noted that for the special case of $d = \lambda/4$, the expression in Eq. 15 is equivalent to the expression for loss given by Dragon [22]

$$\alpha = \frac{R_s}{2Z_0} \frac{\chi_m^2}{k^2 a^3} \left(\frac{1 - \frac{t}{p} + \frac{\lambda}{4p}}{(1 - t/p)^2} + \alpha_2 \right) \tag{16}$$

where $\alpha_2 \approx 1$ for groove shapes with $t/p > 0.1$.

4 Simulations in HFSS

In order to verify the analytical calculations predicting extremely low-loss propagation of the HE_{11} mode in corrugated waveguides, we have employed

the High Frequency Structure Simulator (HFSS) code. Measurement of the propagation loss for the HE_{11} mode at the optimum wavelength is dominated by experimental error from the presence of higher order modes or the experimental setup. Additionally, the fabrication of the corrugated waveguide can lead to non-ideal groove geometries that are trapezoidal, triangular or sinusoidal, instead of rectangular which are not accounted for in Eq. 15. Proper simulation of these highly overmoded waveguides has proved difficult due to the large physical size and very small power loss involved. However, the idealized physical geometry of a linear corrugated waveguide is highly symmetric. In the direction perpendicular to propagation, the HE_{11} mode has fourfold symmetry, and in the direction of propagation, the waveguide is symmetric over the geometry of one groove. Using HFSS with the proper symmetry conditions and applying a phase advance along the direction of propagation, the HE_{11} mode can be analyzed for a variety of groove shapes and frequencies. The magnitude of the electric field in the transverse plane of the corrugated waveguide and at a variety of frequencies is shown in Fig. 5. As seen in Fig. 5, the profile of the HE_{11} mode is significantly distorted when the frequency of operation is not well matched to the corrugation depth, in close agreement with [53]. The distortion in the field profile is due to the frequency dependent impedance of the corrugation leading to increased ohmic losses at lower frequencies. At the $\lambda/4$ condition, the HE_{11} mode is linearly polarized with the direction of the electric field labeled in Fig. 5d. As the frequency is lowered, the HE_{11} mode becomes distorted and is no longer linearly polarized, which would lead to mode conversion if coupling into the transmission line with a Gaussian beam, effectively limiting the bandwidth of the transmission line. The ohmic losses determined by the HFSS computer modeling for the rectangular groove shape (blue dots) are shown in Fig. 4 and are consistent with our model (solid line).

The machining process for the corrugations can lead to deviations from the ideal rectangular groove shape. These deformations, in the form of trape-

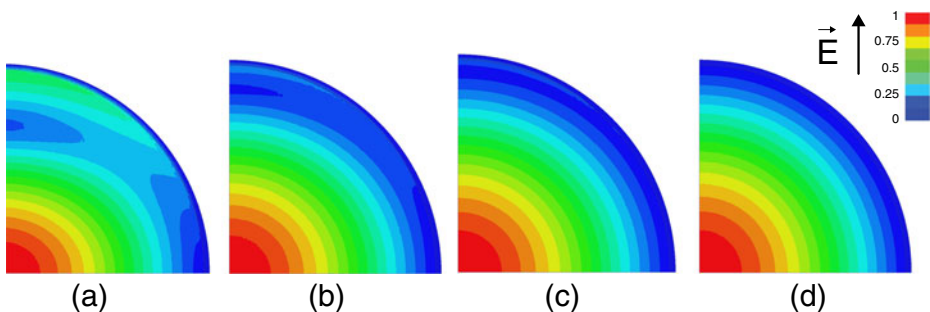


Fig. 5 The magnitude of the electric field from HFSS simulations for one period of a rectangular corrugation with $a = 9.5$ mm, $d = 0.227$ mm, $p = 0.3175$ mm, $t/p = 0.5$ and ideal brass conductivity at **a** 105 GHz, **b** 158 GHz, **c** 250 GHz and **d** 330 GHz.

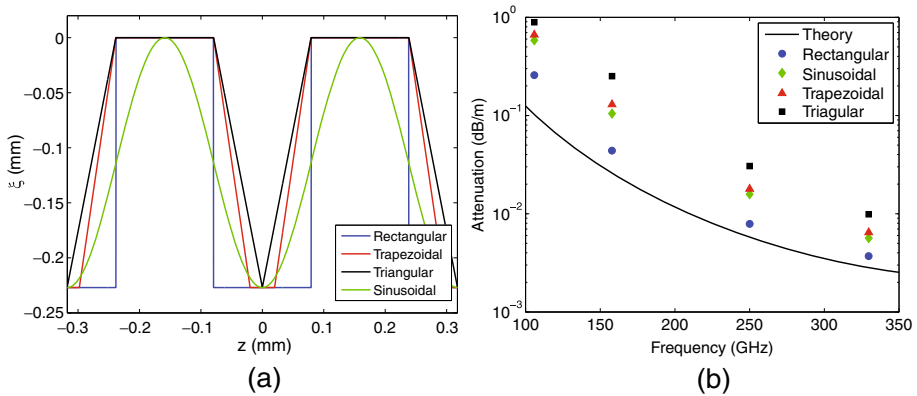


Fig. 6 (a) Groove shapes simulated in HFSS with $d = 0.227$ mm and $p = 0.3175$ mm given in the groove coordinate system (ξ, z) used in Fig. 1. (b) Ohmic losses in corrugated waveguide simulated in HFSS compared to the impedance approximation method.

zoidal, sinusoidal and triangular groove shapes, were found to increase ohmic losses for the corrugated waveguide. Similar deformations also affect the loss on grooved surfaces for diffraction gratings and polarizers [55]. Numerical simulations were performed for the groove shapes shown in Fig. 6a. The increase in ohmic losses for non-ideal groove shapes results from two effects: alteration of the fields on the surface of the groove and decrease of the effective groove depth relative to the actual depth causing an adjustment to the impedance approximation. Expanding the groove shape in a Fourier series and comparing the weight of the first Fourier term accurately predicts which groove shapes result in higher ohmic losses. Adjusting the groove depth can be used to compensate for the transmission losses for non-rectangular shapes. The effective depth of the grooves (shown in Fig. 6a) is listed in Table 1 for various corrugation shapes.

The ohmic losses calculated from the analytical theory and HFSS are shown in Fig. 6b, with the rectangular (blue dots), trapezoidal (red triangles), sinusoidal (green diamonds) and triangular (black squares) groove shapes. The theoretical attenuation calculated with HFSS of the rectangular groove shapes is in very good agreement with the analytical model (black line). Variations to the groove shape result in increased ohmic losses for the same frequency. As predicted in Table 1 and shown in Fig. 6b, the trapezoidal and sinusoidal

Table 1 Corrugation shape depth correction.

Shape	$d_{\text{effective}}$ (normalized)
Rectangular	1.00
Trapezoidal	0.733
Triangular	0.565
Sinusoidal	0.785

grooves show similar levels of ohmic losses, with the triangular shape resulting in the largest increase of attenuation.

5 Fabrication of helically-tapped transmission line components

As the frequency of the waves on the transmission line moves further into the THz regime, fabrication of individual corrugations becomes more difficult and expensive, requiring special tools and dedicated setups [18], but could be performed with relative ease using a helical tap. However, the groove shape in a helically-tapped waveguide does not produce the ideal rectangular groove shape and could result in increased ohmic losses. The simulations discussed in the previous section indicate that there are acceptable non-rectangular groove shapes which a helical tap is capable of tapping. To test this approach, a 4.5 m long transmission line optimized for operation at 330 GHz was constructed from fifteen 19 mm ID 30 cm long brass tubing sections tapped with an 80 grooves per inch (3.15/mm) tap. Brass was chosen as the waveguide material due to its hardness for fine machining and good conductivity. The tap thread before and after machining and the resulting corrugations were examined under magnification as shown in Fig. 7a. The corrugations mirror the shape of the cutting thread looking approximately trapezoidal and with the cut groove narrower than the wall between. The depth of the cutting thread wore down about 10% over the course of fabrication. Images of the grooves indicate $d = 0.227$ mm, $p = 0.318$ mm and $t = p/2$. The trapezoidal groove shape in Fig. 7a corresponds to the trapezoidal groove shown in Fig. 6a and simulated in Fig. 6b. Polarization rotation, which is a concern for helically-grooved waveguide,

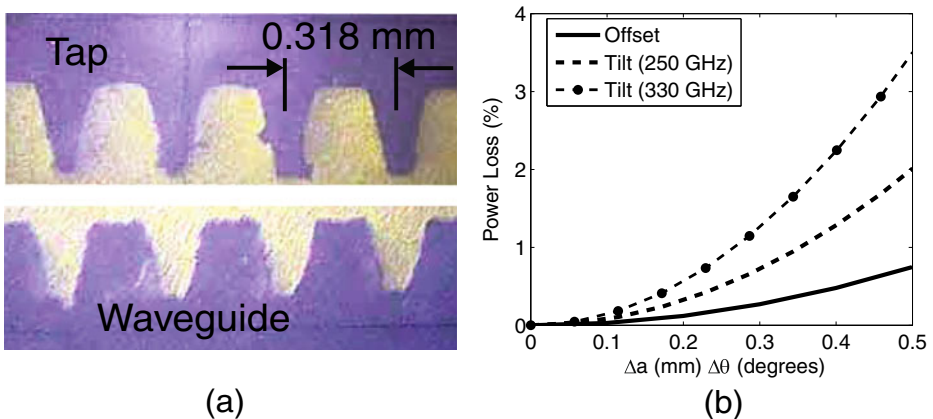


Fig. 7 (a) Photos of the 330 GHz tap and waveguide cross sections. Chips from cutting are present on the second tap tooth from left. (b) Theoretical prediction of power loss due to axial offset (*black line*) and tilts (*dashed and dashed/dotted lines*) at waveguide junctions for the 19 mm diameter 330 GHz corrugated waveguide.

becomes less of an issue at higher frequencies because of the inverse frequency squared scaling. The rotation angle in radians can be estimated by

$$\psi \cong \left(\frac{2.405}{ka} \right)^3 \frac{Lp}{\lambda a} \quad (\text{radians}) \quad (17)$$

where L is the waveguide length [23]. For our waveguide parameters, the rotation is estimated as $0.1^\circ/\text{m}$ at 330 GHz, which is not sufficient to cause a problem for DNP experiments.

The theoretical prediction for offset and tilt losses calculated using Eqs. 5 and 6 for a single joint of our transmission line is shown in Fig. 7b. Errors in successive joints will increase the offset and tilt losses. Even with relatively large offsets (black line) a very modest power loss would be observed; however, the setup is extremely sensitive to tilts (dashed and dashed/dotted lines). To mitigate these effects, collars are placed at each waveguide joint which provide concentricity and angular alignment.

6 Straight waveguide measurements

The predicted loss in a straight section of waveguide is extremely low, limiting the possible experimental methods for measuring the loss. To aid in this process, measurements were taken using a vector network analyzer (VNA) around 250 GHz due to the availability in our laboratory of a high quality fundamental rectangular waveguide to 19 mm ID corrugated waveguide transition. The HE_{11} mode was obtained from the VNA WR-3 fundamental rectangular waveguide by a series of waveguide components consisting of a rectangular to circular transition, a smooth to corrugated waveguide transition, a corrugated conical horn, and an acrylic up taper to the 19 mm ID corrugated waveguide. In a previous measurement [56], the mode content produced by this setup was determined with great accuracy. The VNA (Agilent E8363B with millimeter-wave VNA extender V03VNA2-T/R) setup for transmission line losses and radiated field measurements is shown in Fig. 8a with the VNA extender head and up tapers in the lower left of the photo. At the other end of the waveguide there is an automated beam profile scanner. A schematic of this setup is shown in Fig. 8b with the scanner replaced by a removable short or load. A 2 m section of straight waveguide was used to bring the HE_{11} mode from the launcher to the scanner setup. The magnitude and phase of the radiated beam were recorded for spatial scans at 7, 10 and 13 cm distances from the waveguide aperture. Two methods, a phase retrieval code [57] and direct magnitude/phase measurements, showed that an HE_{11} mode purity of $94.2 \pm 0.3\%$ was generated at 250 GHz. The detailed mode content of the microwave fields in the corrugated waveguide is listed in Table 2 with the decomposition performed using a linearly polarized basis set [46] where the LP_{01} mode is the linearly polarized HE_{11} mode. The large HE_{11} mode content allows the use of this setup to perform transmission loss measurements to test the quality of the

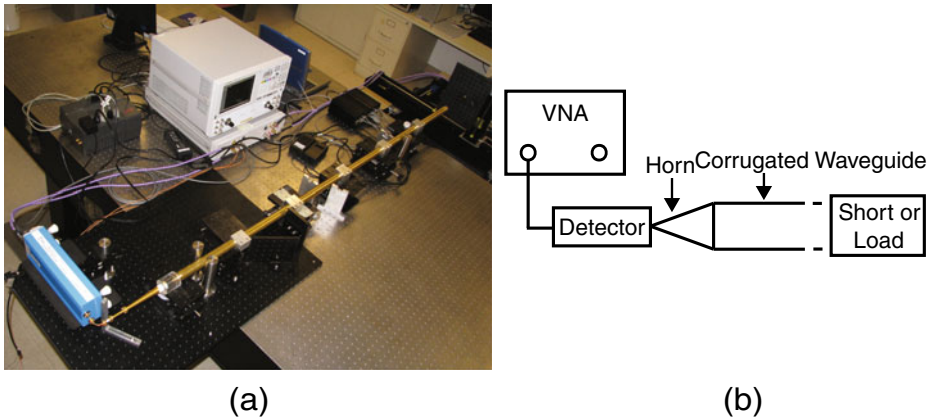


Fig. 8 (a) VNA setup for 330 GHz waveguide transmission line loss measurements. (b) Schematic of the setup for transmission line losses with removable short or load.

transmission line and to make a comparison to the theoretical and numerical calculations from Sections 3 and 4.

Validation of the theoretical calculation for the loss was accomplished with two methods to measure transmission losses. In the first method, a heterodyne radiometer and liquid nitrogen cooled blackbody (Eccosorb) were used to measure insertion losses relative to thermal noise over the band 248 ± 4 GHz using techniques previously described [1]. The attenuation in the waveguide was determined by comparing the relative intensity of the receiver noise measurement with the addition of waveguide sections, up to a total of 3 m. In the second method, a VNA was used to perform calibrated S_{11} measurements to determine the ohmic loss in the system [58]. The S_{11} measurements entailed short and matched load (radiation into free space) measurements for every added section of the overmoded waveguide. Reflection measurements are preferable to transmission for measuring very small losses over a distance of several meters because the measurement setup for the detector can remain immobile while sections of waveguide are added. This removes a significant source of error introduced by flexing cables and making connections. Several challenges present themselves when performing S_{11} measurements in the overmoded waveguide including Fabry–Pérot resonances caused by small mismatches and mode beating. Fabry–Pérot effects were removed by taking

Table 2 Modes at the aperture of the corrugated waveguide.

Power				Phase (radians)			
LP_{mn}	n = 1	n = 2	n = 3	LP_{mn}	n = 1	n = 2	n = 3
m = 0	0.942	0.040	0.003	m = 0	-1.69	-1.77	0.06
m = 1	0.007	<0.001	<0.001	m = 1	2.11	-	-
m = 2	0.004	<0.001	<0.001	m = 2	1.42	-	-

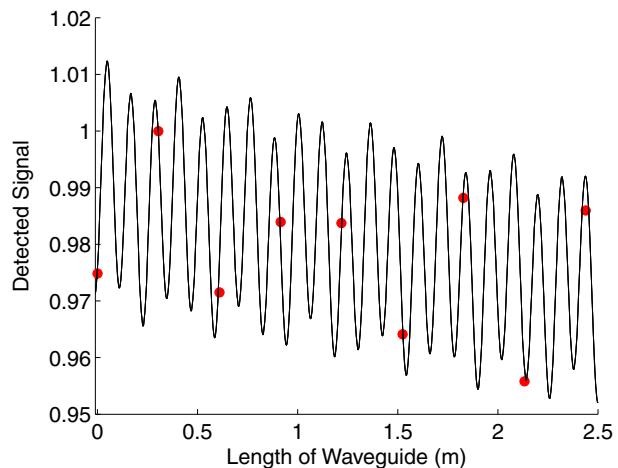
measurements over the 240–260 GHz range and filtering the oscillations on the measured signal. The treatment for mode beating, if the HE₁₁ mode is dominant, can be generalized to express the relationship between the detected power and the relative phase of various higher order modes with respect to the HE₁₁ mode. With 94.2% of the power in the HE₁₁ mode, the beating can be described by

$$P_D = |A_{01}e^{-\alpha_{01}z} + A_{\text{HOM}}e^{i(\phi_{\text{HOM}})}e^{-\alpha_{\text{HOM}}z}|^2 \tag{18}$$

where P_D is the detected power, A_{mn} is the amplitude given in Table 2, α_{mn} is the attenuation constant and HOM designates the higher order mode index that is being considered. The relative phase, $\phi_{\text{HOM}} = 2L(k_{01z} - k_{\text{HOM}z})$, between the modes is determined by the phase of the reconstructed mode content, shown in Table 2, back propagated to the measurement plane for the straight waveguide measurements. The measured and calculated P_D for the system is shown in Fig. 9. The calculated P_D is based on the power and phase in the 5 lowest higher order modes, with the attenuation in the waveguide as the only free variable, and is determined from the best fit between the measured and calculated transmitted power.

The transmission as a function of length for the straight waveguide measurements, which is computed from the S_{11} measurements [6, 58], is shown in Fig. 10a. Measurements in Fig. 10a were independently repeated 5 times, with the mean of the measurements shown with black dots and one standard deviation is marked with error bars for each added section of waveguide. The attenuation, α , is determined by a best fit for $e^{-\alpha z}$. The measured insertion losses, plotted in Fig. 10b, are 0.047 ± 0.01 and 0.029 ± 0.009 dB/m for the radiometer and VNA, respectively. The measurements are in reasonable agreement with one another and with the theoretical estimate. The difference between the VNA measurement and HFSS model can be explained by adjusting the bulk resistivity by a factor of 2 (or $\sqrt{2}$ for the surface resistance).

Fig. 9 Predicted (black line) and measured (red dot) signal from the VNA as a function of waveguide length.



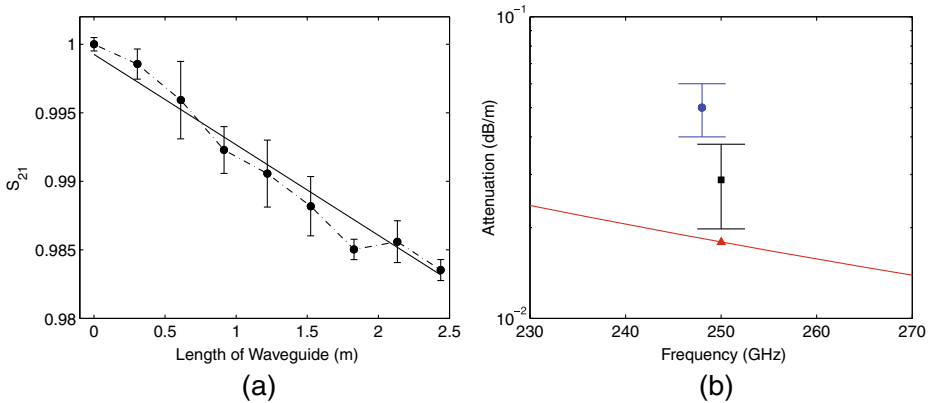


Fig. 10 (a) Measured transmission through 19 mm ID corrugated waveguide at 250 GHz as a function of waveguide length. (b) HE_{11} waveguide transmission loss measurements (blue dot: radiometer, black square: vector network analyzer) and HFSS model (red triangle and line: trapezoidal groove) for ideal brass conductivity and $a = 9.5$ mm.

The resulting losses of $\sim 3\%$ for the complete 4.5 m straight waveguide length are acceptable for the intended application. Consequently, using a tap to save fabrication costs of corrugated waveguide does not cause the quality of the waveguide to suffer, with deeper groove depth compensating for non-ideal rectangular shape.

7 Discussion and conclusions

The transmission of THz radiation over significant distances has proven to be a challenge for systems requiring high efficiencies. Additional problems have surfaced when considering high-power THz radiation where ohmic losses or mode conversion can lead to physical damage to the transmission line or load. Overmoded corrugated waveguides have proved to be a reliable technique with regards to their low-loss nature and ability to handle high-powers. Corrugated waveguides routinely achieve losses below 0.01 dB/m for the lowest order HE_{11} mode. However, their overmoded nature requires precise excitation and very accurate physical alignment of the transmission line to avoid severe mode conversion which leads to increased ohmic losses and a poorer beam quality output. Additionally, corrugated waveguides do have a large, but limited bandwidth due to the frequency-dependent nature of the corrugations. Frequencies far below the optimized condition of $d \approx \lambda/4$ experience increased ohmic losses and the HE_{11} mode is no longer linearly polarized. Bragg reflections occur for higher frequencies when $d \approx n\lambda/2$, where $n = 1, 2, 3, \dots$ is an integer. At frequencies well above 1 THz overmoded corrugated waveguides remain an unproven technology. However, with a minimum reported loss of 1 dB/m alternate forms of transmission lines above

1 THz, have not achieved comparable low-losses. With improved machining and the availability of free space Gaussian beams, overmoded corrugated waveguides could extend into this regime. Corrugated waveguides that require individual machining of grooves are costly and complex when frequencies approach the THz range. However, helically-tapped waveguides are much simpler to fabricate and have corrugations that are very effective in low-loss transmission. Typical designs for overmoded corrugated waveguides operate with similar corrugation dimensions with $d \approx \lambda/4$, $p \approx \lambda/3$ and $t \approx p/2$. We can write Eq. 10 as

$$\alpha = \frac{\lambda^{1.5}}{a^3} C_{OM} \tag{19}$$

where we took $R_S \propto 1/\sqrt{\lambda}$ and C_{OM} is a constant, shown in Table 3 for a variety of metals, scaled from the measurements on the brass corrugated waveguide presented in this paper.

From this expression it is evident that these waveguides become more favorable at higher frequencies as the wavelength gets shorter. With their behavior being extremely dependent on the waveguide radius, it is also possible to drastically improve performance for long transmission lines with larger diameter waveguide. Additionally, this expression provides a realistic expectation for the HE_{11} mode loss on a transmission line. We should also note that for both the TE_{10} mode in rectangular waveguide and TE_{11} mode in circular waveguide the attenuation has a starkly different dependence, $\alpha \propto \lambda^{-0.5}/a$, where a is the long dimension in rectangular waveguide and the radius in circular waveguide. As frequencies push into the THz regime, these modes require prohibitively large cross sections for many applications to maintain a reasonable attenuation coefficient. An alternative is to use the TE_{01} mode in smooth-walled circular waveguides which has a similar dependence to the HE_{11} mode, but this mode is difficult to couple to free space Gaussian beams.

Transmission of THz radiation is a growing area of research due to the increasing availability of THz sources capable of producing a megawatt of average power in the near-THz and 10–100 W in the THz band. The ohmic losses in corrugated waveguides are well understood, with good agreement between theory, simulation and experiments. High quality Gaussian beams that couple efficiently to the HE_{11} mode of the corrugated waveguide are a requirement for low-loss operation. The higher order mode content of the transmission line can produce increased ohmic losses on straight waveguide sections and reduced performance of components such as miter bends and

Table 3 Normalized attenuation coefficient for metallic corrugated waveguide.

	C_{OM} (NP · m ^{0.5})	C_{OM} (dB · m ^{0.5})
Brass	3.94×10^{-5}	3.42×10^{-4}
Al	3.11×10^{-5}	2.70×10^{-4}
Copper	2.03×10^{-5}	1.76×10^{-4}

tapers. Overmoded corrugated transmission lines with high average powers have been successfully implemented on plasma fusion experiments and DNP NMR experiments up to 0.46 THz, and this study shows that they will continue to be of value at higher frequencies.

Acknowledgements This work is supported by the NIH and NIBIB under the Contracts R01-EB004866 and R01-EB001965 and by the US ITER Project managed by Battelle/Oak Ridge National Laboratory.

References

1. P.P. Woskov, V.S. Bajaj, M.K. Hornstein, R.J. Temkin, R.G. Griffin, *IEEE Transactions on Microwave Theory and Techniques*, **53**(6), 1863 (2005)
2. P.P. Woskov, M.K. Hornstein, R.J. Temkin, in *The Joint 30th International Conference on Infrared and Millimeter Waves and 13th International Conference on Terahertz Electronics*, vol. 2 (2005), pp. 563–564
3. E. de Rijk, A. Macor, J.P. Hogge, S. Alberti, J.P. Ansermet, *Rev. Sci. Instrum.* **82**(6), 066102 (2011)
4. G. Denisov, A. Chirkov, V. Belousov, A. Bogdashov, G. Kalynova, D. Sobolev, Y. Rodin, E. Tai, V. Ilin, S. Kornishin, M. Kulygin, V. Malygin, E. Soluyanov, V. Parshin, M. Shmelev, *Journal of Infrared, Millimeter and Terahertz Waves* **32**(3), 343 (2011)
5. A. Bogdashov, V. Belousov, A. Chirkov, G. Denisov, V. Korchagin, S. Kornishin, E. Tai, *Journal of Infrared, Millimeter and Terahertz Waves* **32**(6), 823 (2011)
6. P. Woskov, E. Nanni, M. Shapiro, S. Jawla, J. Hummelt, R. Temkin, A. Barnes, in *36th International Conference on Infrared Millimeter and Terahertz Waves (IRMMW-THz)*, (2011)
7. V.P. Denysenkov, M.J. Prandolini, A. Krahn, M. Gafurov, B. Endeward, T.F. Prisner, *Applied Magnetic Resonance* **34**(3), 289 (2008)
8. T. Idehara, K. Kosuga, L. Agusu, R. Ikeda, I. Ogawa, T. Saito, Y. Matsuki, K. Ueda, T. Fujiwara, *Journal of Infrared, Millimeter and Terahertz Waves* **31**(7), 775 (2010)
9. K.R. Thurber, W.M. Yau, R. Tycko, *J. Mag. Res.* **204**(2), 303 (2010)
10. B.D. Armstrong, D.T. Edwards, R.J. Wyld, S.A. Walker, S. Han, *Physical Chemistry Chemical Physics* **12**(22), 5920 (2010)
11. P.A.S. Cruickshank, D.R. Bolton, D.A. Robertson, R.I. Hunter, R.J. Wyld, G.M. Smith, *Rev. Sci. Instrum.* **80**(10), 103102 (2009)
12. K. Ohkubo, S. Kubo, H. Idei, M. Sato, T. Shimozuma, Y. Takita, *International Journal of Infrared and Millimeter Waves* **18**(1), 23 (1997)
13. P. Bhartia, I. Bahl, *Millimeter Wave Engineering and Applications* (John Wiley and Sons, Inc., New York, NY, 1984)
14. M.K. Thumm, W. Kasperek, *IEEE Transactions on Plasma Science*, **30**(3), 755 (2002)
15. R.W. Callis, W.P. Cary, R. Ellis, Y.A. Gorelov, H.J. Grunloh, J. Lohr, J.J. Peavy, R.I. Pinsker, D. Ponce, R. Prater, in *The 29th IEEE International Conference on Plasma Science*, (2002), p. 294
16. F. Leuterer, M. Beckmann, H. Brinkschulte, F. Monaco, M. München, F. Ryter, H. Schütz, L. Empacher, G. Gantenbein, W. Förster, W. Kasperek, P. Schüller, K. Schwörer, A. Borchegowski, A. Fix, V. Ilin, L. Popov, V. Sigalaev, E. Tai, *Fusion Engineering and Design* **53**(1–4), 485 (2001)
17. H. Idei, S. Kubo, T. Shimozuma, M. Sato, K. Ohkubo, Y. Yoshimura, Y. Takita, S. Kobayashi, S. Ito, Y. Mizuno, K. Tsumori, K. Ikeda, T. Notake, T. Watari, O. Kaneko, A. Komori, H. Yamada, P.C. de Vries, M. Goto, K. Ida, S. Inagaki, S. Kado, K. Kawahata, T. Kobuchi, T. Minami, J. Miyazawa, T. Morisaki, S. Morita, S. Murakami, S. Muto, Y. Nagayama, H. Nakanishi, K. Narihara, B.J. Peterson, S. Sakakibara, H. Sasao, K. Sato, K. Tanaka, Y. Takeiri, K.Y. Watanabe, I. Yamada, O. Motojima, M. Fujiwara, *Fusion Engineering and Design* **53**(1–4), 329 (2001)
18. J.L. Doane, *Fusion Science and Technology* **53**, 159 (2008)

19. J.L. Doane, R.A. Olstad, *Fusion Science and Technology* **53**(1), 39 (2008)
20. F. Gandini, et al., *Fusion Science and Technology* **59**(4), 709 (2011)
21. E. Choi, M. Shapiro, J. Sirigiri, R. Temkin, *Journal of Infrared, Millimeter and Terahertz Waves* **30**(1), 8 (2009)
22. C. Dragone, *IEEE Transactions on Microwave Theory and Techniques*, **28**(7), 704 (1980)
23. J.L. Doane, “Propagation and mode coupling in corrugated and smooth-wall circular waveguides”, *Infrared and millimeter waves* (Academic Press, Inc. Orlando, FL) vol. 13 (A86-37151 17-33) (1985), pp. 123–170
24. O. Mitrofanov, R. James, F.A. Fernandez, T.K. Mavrogordatos, J.A. Harrington, *IEEE Transactions on Terahertz Science and Technology*, **1**(1), 124 (2011)
25. G. Gallot, S.P. Jamison, R.W. McGowan, D. Grischkowsky, *J. Opt. Soc. Am. B* **17**(5), 851 (2000)
26. O. Mitrofanov, J.A. Harrington, *Opt. Express* **18**(3), 1898 (2010)
27. R. Mendis, D. Grischkowsky, *J. Appl. Phys.* **88**, 4449 (2000)
28. L.J. Chen, H.W. Chen, T.F. Kao, J.Y. Lu, C.K. Sun, *Opt. Lett.* **31**(3), 308 (2006)
29. K. Wang, D.M. Mittleman, *Nature* **432**(7015), 376 (2004)
30. R. Mendis, D.M. Mittleman, *J. Opt. Soc. Am. B* **26**(9), A6 (2009)
31. A. Hassani, A. Dupuis, M. Skorobogatiy, *Opt. Express* **16**(9), 6340 (2008)
32. M. Goto, A. Quema, H. Takahashi, S. Ono, N. Sarakura, *Japanese Journal of Applied Physics* **43**(2B), 317 (2004)
33. B. Bowden, J.A. Harrington, O. Mitrofanov, *Applied Physics Letters* **93**(18), 181104 (2008)
34. J. Oosterbeek, A. Bürger, E. Westerhof, d.M. Baar, v.d.M. Berg, W. Bongers, M. Graswinckel, B. Hennen, O. Kruijt, D. Thoen, R. Heidinger, S. Korsholm, F. Leipold, S. Nielsen, *Rev. Sci. Instrum.* **79**(9), 093503 (2008)
35. W.A. Bongers, et al., *Fusion Science and Technology* **55**(2), 188 (2009)
36. M. Henderson, et al., *Nuclear Fusion* **48**(5), 054013 (2008)
37. W. Rowan, M. Austin, J. Beno, R. Ellis, R. Feder, A. Ouroua, A. Patel, P. Phillips, *Rev. Sci. Instrum.* **81**(10), 10D935 (2010)
38. M. Austin et al., in *Proceedings of the Fifteenth Joint Workshop on Electron Cyclotron Emission and Electron Cyclotron Resonance Heating: Yosemite National Park, California, USA* (2009), pp. 170–177
39. G.R. Hanson, J.B. Wilgen, T.S. Bigelow, S.J. Diem, T.M. Biewer, *Rev. Sci. Instrum.* **81**, 10D920 (2010)
40. E.A. Nanni, A.B. Barnes, R.G. Griffin, R.J. Temkin, *IEEE Transactions on Terahertz Science and Technology*, **1**(1), 145 (2011)
41. M.K. Hornstein, V.S. Bajaj, R.G. Griffin, K.E. Kreischer, I. Mastovsky, M.A. Shapiro, J.R. Sirigiri, R.J. Temkin, *IEEE Transactions on Electron Devices*, **52**(5), 798 (2005)
42. V. Bajaj, C. Farrar, M. Hornstein, I. Mastovsky, J. Viereg, J. Bryant, B. Elena, K. Kreischer, R. Temkin, R. Griffin, *J. Mag. Res.* **160**, 85 (2003)
43. A.C. Torrezan, M.A. Shapiro, J.R. Sirigiri, R.J. Temkin, R.G. Griffin, *IEEE Transactions on Electron Devices*, **58**(8), 2777 (2011)
44. M. Rosay, L. Tometich, S. Pawsey, R. Bader, R. Schauwecker, M. Blank, P.M. Borchard, S.R. Cauffman, K.L. Felch, R.T. Weber, R.J. Temkin, R.G. Griffin, W.E. Maas, *Physical Chemistry Chemical Physics* **12**(22), 5850 (2010)
45. I. Ogawa, T. Idehara, M. Pereyaslavets, W. Kasperek, *International Journal of Infrared and Millimeter Waves* **20**(4), 543 (1999)
46. E.J. Kowalski, D.S. Tax, M.A. Shapiro, J.R. Sirigiri, R.J. Temkin, T.S. Bigelow, D.A. Rasmussen, *IEEE Transactions on Microwave Theory and Techniques*, **58**(11), 2772 (2010)
47. J.L. Doane, C.P. Moeller, *International Journal of Electronics* **77**(4), 489 (1994)
48. E.A. Nanni, A.B. Barnes, Y. Matsuki, P.P. Woskov, B. Corzilius, R.G. Griffin, R.J. Temkin, *J. Mag. Res.* **210**(1), 16 (2011)
49. I. Ogawa, T. Idehara, M. Myodo, H. Ando, D. Wagner, M. Thumm, in *Joint 31st International Conference on Infrared Millimeter Waves and 14th International Conference on Terahertz Electronics*, (2006), pp. 552–552
50. Y. Matsuki, H. Takahashi, K. Ueda, T. Idehara, I. Ogawa, M. Toda, H. Akutsu, T. Fujiwara, *Physical Chemistry Chemical Physics* **12**(22), 5799 (2010)
51. R.J. Temkin, A.B. Barnes, R.G. Griffin, S. Jawla, E. Nanni, A.C. Torrezan, in *Third International Symposium on Dynamic Nuclear Polarization* (2011)

52. R. Temkin, A. Barnes, R. Griffin, S. Jawla, I. Mastovsky, E. Nanni, M. Shapiro, A. Torrezan, P. Woskov, in *36th International Conference on Infrared Millimeter and Terahertz Waves (IRMMW-THz)*, (2011)
53. P.J.B. Clarricoats, A.D. Olver, *Corrugated horns for microwave antennas*. IEEE Electromagnetic Waves Series (London, U.K.: Peter Peregrinus, 1984)
54. P.J.B. Clarricoats, A.D. Olver, S.L. Chon, Institution of Electrical Engineers, Proceedings **122**(11), 1173 (1975)
55. B. Plaum, E. Holzhauer, C. Lechte, *Journal of Infrared, Millimeter and Terahertz Waves* pp. 1–14 (2011)
56. S.K. Jawla, E.A. Nanni, M.A. Shapiro, P.P. Woskov, R.J. Temkin, Mode content determination of terahertz corrugated waveguides using experimentally measured radiated field patterns, *IEEE Transactions on Plasma Science* (2012)
57. S. Jawla, J.P. Hogge, S. Alberti, T. Goodman, B. Piosczyk, T. Rzesnicki, *IEEE Transactions on Plasma Science*, **37**(3), 414 (2009)
58. E.J. Kowalski, E.A. Nanni, M.A. Shapiro, J.R. Sirigiri, R.J. Temkin, T.S. Bigelow, D.A. Rasmussen, in *IEEE International Vacuum Electronics Conference (IVEC)*, (2010), pp. 335–336